Optimal Design of THz NRD Rat-Race Circuit Using Function Expansion Based Topology Optimization Method With CMA-ES

Md. Iquebal Hossain Patwary, Tahir Bashir, Akito Iguchi, *Member, IEEE*, and Yasuhide Tsuji, *Senior Member, IEEE*

***Abstract*—Rat-race circuit devices are crucial components in the design of THz-wave circuits. Although nonradiative dielectric (NRD) waveguides having simple structures and extremely low loss are promising platforms for THz-wave circuits, it may difficult to realize conventional rat-race devices in NRD platform due to the appearance of unwanted LSE_{01} mode in the output ports. Therefore, optimal design of these devices is very essential for THz-wave circuit applications. In this paper, we present topology optimal design of THz NRD rat-race circuit based on function expansion method and covariance matrix adaptation evolution strategy (CMA-ES). The proposed method overcomes the difficulty of appearing unwanted LSE_{01} mode in the output ports, thus the optimized devices achieved the significant improvement in the device performance in comparison with that of conventional NRD rat-race devices. In addition to the NRD rat-race circuit, a 90° hybrid device is also designed in order to confirm the validity of the proposed design approach. A thorough discussion of the fabrication tolerance of proposed devices has also been conducted in detail.**

***Index Terms*—Nonradiative dielectric (NRD) waveguide, rat-race circuit, 90° hybrid device, topology optimization, function expansion method, covariance matrix adaptation evolution strategy (CMA-ES), full-vectorial finite element method.**

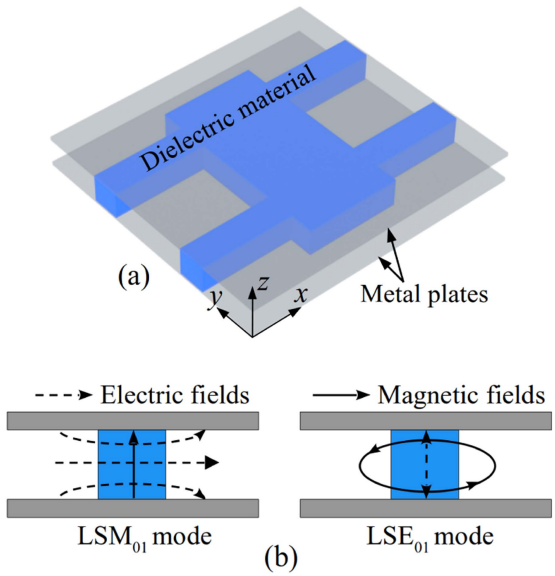

Fig. 1. (a) Image of NRD guide device, and (b) nonradiative propagation modes of the NRD guide.

I. Introduction

THE rapid increase in the amount of data transmission rate over the internet in recent years allows terahertz-wave band [1] to be investigated actively and meet the demand for high-speed, large-capacity optical communications. The THz band has a wide range of applications in numerous scientific and technological fields, such as communication, absorbers, biotechnology, spectroscopy, imaging and sensing systems due to its large bandwidth and high transmission rate [2], [3], [4], [5], [6], [7], [8], [9]. However, transmission in this frequency spectrum has some limitations and propagation loss has become a great concern among them. Therefore, development of THz-wave circuits with compact and low-loss waveguide devices is of the utmost significance. To meet this demand, various waveguides have been developed in recent years, including rectangular waveguides [10], parallel plate waveguides (PPW) [11], parallel plate dielectric waveguides (PPDW) [12], [13] and non-radiative dielectric waveguides (NRD) [14], [15]. Among these waveguides, NRD guides are drawing significant attention for THz-wave integrated circuits due to their non-radiative nature and lack of out-of-plane radiation thus experience extremely low THz loss compared to the other waveguides [16], [17]. The NRD guide has a simple structure consists of a dielectric material sandwiched between two parallel metal plates with spacing less than half wavelength (λ/2) and supports two orthogonal modes, LSM and LSE as shown in Fig. 1.

Rat-race circuit devices serve as significant components of THz-wave integrated circuit development owing to their strong port isolation and broad bandwidth in power splitting distribution [18]. Although these devices have been widely studied for RF and microwave applications such as phase shifters, mixers, energy harvesting, wireless systems, sensors and comparators [19], [20], [21], [22], [23], they have not been well discussed for THz-wave range where typical microstrip-based

Manuscript received 1 May 2024; revised 2 June 2024; accepted 4 June 2024. Date of publication 7 June 2024; date of current version 18 June 2024. This work was supported by JSPS (Japan) KAKENHI under Grant 21K04169. *(Corresponding author: Yasuhide Tsuji.)*

Md. Iquebal Hossain Patwary, Akito Iguchi, and Yasuhide Tsuji are with the Muroran Institute of Technology, Muroran 060-8585, Japan (e-mail: y-tsuji@mmm.muroran-it.ac.jp).

Tahir Bashir is with the Nanjing University of Posts and Telecommunications, Nanjing 210046, China.

Digital Object Identifier 10.1109/JPHOT.2024.3411115

rat-race circuits are difficult to fabricate due to their extreme transmission loss. Thus, the NRD guide appears to be more appropriate in terms of designing compact and low-loss THz rat-race circuit devices, though conventional rat-race devices in NRD platform may be difficult to realize due to the appearance of unwanted LSE_{01} mode in the output ports. Therefore, to overcome this difficulty it is imperative that these THz NRD rat-race circuits be designed optimally using an efficient optimal design technique.

In recent years, various kinds of optimal design techniques have been intensively studied based on size optimization, shape optimization, mosaic optimization and topology optimization for the efficient design of high performance optical and photonic devices [24], [25], [26], [27], [28], [29], [30], [31], [32]. Among these optimization techniques, topology optimization method has attracted a lot of attention because of its highest level of design flexibility, which may produce arbitrary unique structures regardless of any geometric topology. Previously, function expansion based topology optimization has been presented in the literature, where different evolutionary approaches and gradient method are usually used as the solution search methods [33], [34], [35], [36]. The gradient approach with adjoint variable method (AVM) may have a high search efficiency, but it frequently tends to fall into a local optimum, thus, in order to get the global optimum, a suitable initial solution is needed. On the other hand, even if a global solution can be found by evolutionary approaches, search efficiency is not necessarily high.

In this paper, we propose optimal design of THz NRD rat-race circuit using function expansion based topology optimization method, where covariance matrix adaptation evolution strategy (CMA-ES) [37] is utilized as the solution search algorithm. In CMA-ES, reliable and efficient solution search is possible compared with gradient methods and evolutionary approaches using a multivariate normal distribution. Here, conventional NRD rat-race circuit and modified branch NRD rat-race with triangle cut consideration and rectangle cut consideration are initially studied, and it is demonstrated that the intended output results can not be achieved. Then, using the proposed methodology, NRD rat-race circuit is designed to show that the proposed device can achieve the desired device performance by overcoming the difficulty of appearing unwanted LSE_{01} mode in the output ports. A 90° hybrid device is also designed in addition to the NRD rat-race circuit to confirm the effectiveness of the proposed design approach. Both the NRD rat-race and the 90° hybrid device are further designed for the broadband operation by simply modifying the objective functions and considering them for a range of frequencies within the aimed frequency band. The recently established two-dimensional full-vectorial finite element method (2D-FVFEM) for NRD guide devices is employed here in the propagation analysis of the proposed THz devices [38]. Finally, we demonstrate the fabrication tolerance of the designed devices with regard to the impact of structural deviation on the required phase angle and output power of the device.

II. Design of Conventional NRD Rat-Race Circuit

The conventional rat-race circuit is a four-port reciprocal hybrid device that contains a closed ring with a circumference of 3λ/2 as shown in Fig. 2, mostly used as power divider and combiner [39]. In this paper, we consider the power dividing application for example as seen in the figure, where equal magnitude equal phase and equal magnitude opposite phase in the output ports 3, 4 can be obtained with considering ports 1 and 2 as the input ports, respectively, while nonoperating input port always remains isolated. In this research, we initially designed a conventional NRD rat-race along with the modified branch NRD rat-race and this section presents the results and discussion of these designed devices.

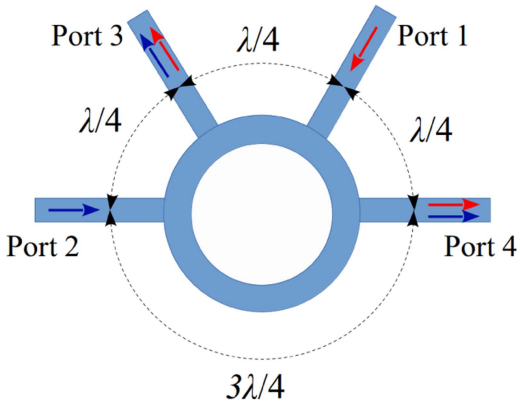

Fig. 2. An example of conventional rat-race circuit with power dividing application.

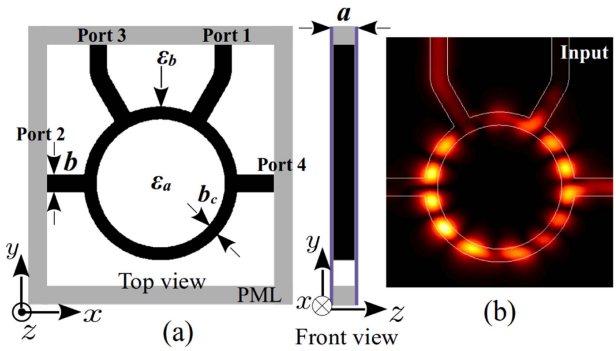

Fig. 3. Conventional rat-race circuit in NRD platform, (a) design setup, (b) propagation field.

A. Conventional NRD Rat-Race

We consider a design setup of conventional NRD rat-race circuit as shown in Fig. 3(a). The design parameters are, spacing between metal plates and width of the dielectric strip, $a = b = 135\,\mu$m, dielectric (polyethylene) permittivity $\varepsilon_b = 2.3$ and air permittivity $\varepsilon_a = 1$. The computational domain is surrounded by the perfectly matched layer (PML) with a thickness of $250\,\mu$m. LSM_{01} mode is used in NRD as the guided mode incident to port 1 and operating frequency is considered 1 THz. The circumference and waveguide width of the closed ring have been optimized simultaneously and are set to, $9\lambda_g/2$ and $b_c = 100\,\mu$ m, respectively. Here, $\lambda_g = 731\,\mu$m is the guided mode wavelength in the closed ring with an effective index of, $n_{\text{eff}} = 0.4099$. Therefore, the calculated ring dimension is set to, inner radius $= 474\,\mu$m

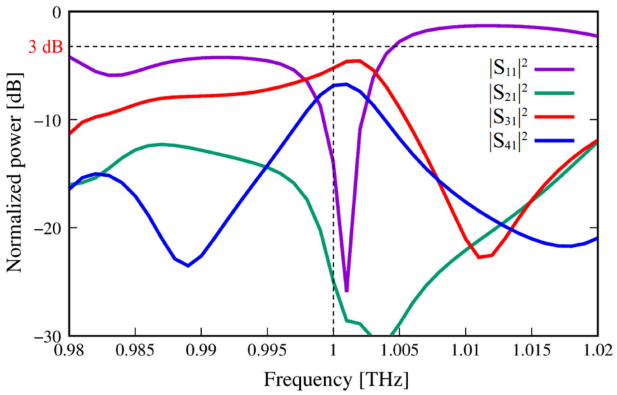

Fig. 4. Frequency characteristics of the designed conventional NRD rat-race circuit.

and outer radius $= 574\,\mu$m. Fig. 3(b) shows the propagation field of the designed NRD rat-race device. In NRD branching waveguide, LSM_{01} mode is often converted into LSE_{01} mode or vice-versa. Therefore, in the figure it is seen that LSE_{01} mode appears in the output ports of the device because of the presence of waveguide branches, thus the desired transmission property could not be obtained. The achieved transmission power (LSM_{01} mode) into the output ports, 3 and 4 at 1 THz are, 30.0% and 20.7%, respectively, whereas maximum of 17.3% LSE_{01} mode appears in the output ports. The frequency characteristics of the device around 1 THz are depicted in Fig. 4, where we can see the transmittance at ports 3 and 4 stands far below the 3 dB line with a reflection of -14 dB.

B. NRD Rat-Race With Modified Branch

The transmission power at the output ports can be improved by modifying the branching waveguide of the conventional NRD rat-race circuit. In this case, two distinct modified branches, one with a rectangle cut and the other with a triangle cut have been taken into consideration. Fig. 5(a) and (b) illustrate the designed rat-race structures with triangle and rectangle cut considerations, respectively. Here, the parameters of branching waveguide have been optimized and are set to, $g = h = 100\,\mu$m is for triangle cut consideration and $g = h = 75\,\mu$m is for rectangle cut consideration. All the other design parameters are set to be same as the previous design example. The propagation fields of the designed modified branch NRD rat-race devices for triangle and rectangle cuts of NRD branches are depicted in Fig. 6(a) and (b), respectively. In the figure we can see that the propagation fields are almost same in both the cases and the achieved transmission power into the ports, 3 and 4 at 1 THz are, 32.8% and 25.4% for triangle cut consideration and 35.2% and 24.5% for rectangle cut consideration. The maximum LSE_{01} mode appears in the output ports for triangle cut consideration is 25.8%, and 23.7% it is for rectangle cut consideration. Although the transmission power is slightly improved by (4-5)%, the LSE_{01} mode in the output ports is partially degraded in both the cases and the transmission improvement is insufficient for the practical application. The frequency characteristics of the device with triangle cut branches

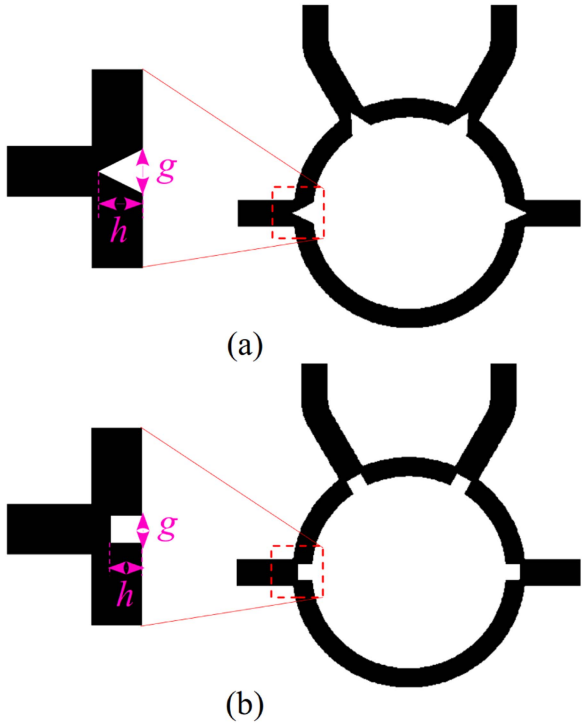

Fig. 5. Modified branch NRD rat-race structure, (a) with triangle cut consideration and (b) with rectangle cut consideration.

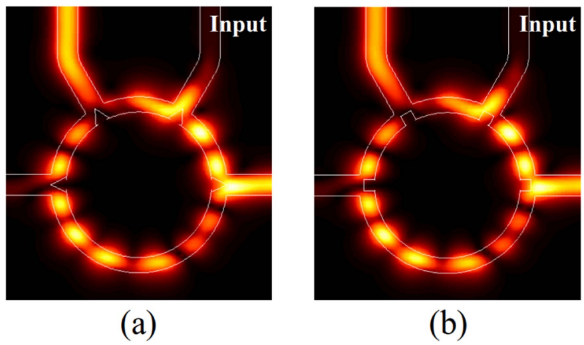

Fig. 6. Propagation fields in the Modified branch NRD rat-race, (a) rat-race with triangle cut and (b) rat-race with rectangle cut.

are shown in Fig. 7(a), whereas Fig. 7(b) shows the frequency characteristics of the device with rectangle cut branches. In accordance with the frequency characteristics, transmittance at ports 3 and 4 still remains significantly below the 3 dB line, despite a minor reduction in reflection of nearly 4 dB. Based on these results, we can conclude that improving the branching waveguide partially improves the performance of the rat-race device, though the unwanted LSE_{01} mode still significantly appears in the output ports. Therefore, the conventional rat-race circuit may difficult to be realized in NRD platform, making the optimal design for these devices crucial.

III. Topology Optimal Design of NRD Rat-Race Circuit

This section presents the topology optimal design method of NRD rat-race devices in terms of structure representation,

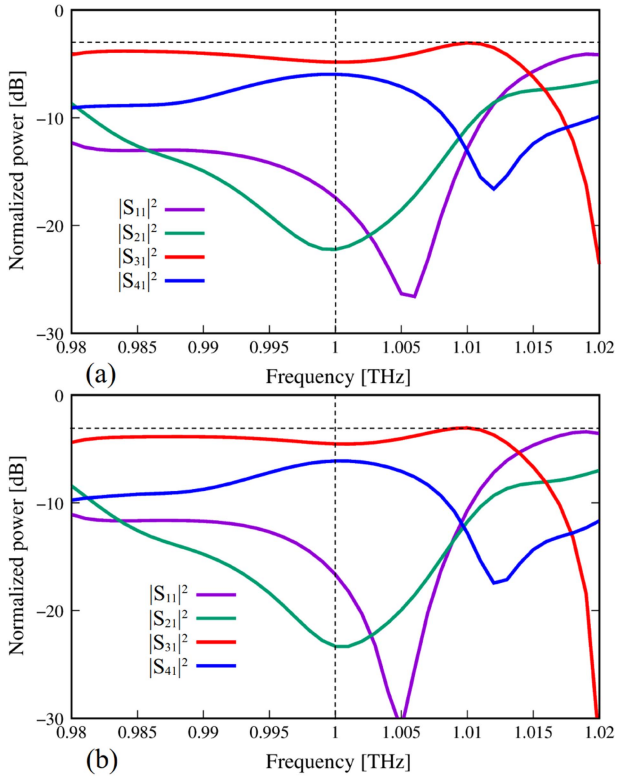

Fig. 7. Frequency characteristics of the designed Modified branch NRD rat-race, (a) with triangle cut consideration and (b) with rectangle cut consideration.

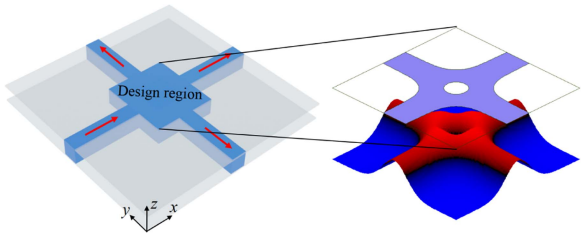

Fig. 8. Problem setting of function expansion based topology optimal design.

optimization of design variables and the propagation analysis during the optimization process.

A. Representation of Structure Using Function Expansion Method

In this paper, the function expansion method is employed for the device structure representation and we consider a problem setting of function expansion based topology optimal design as shown in Fig. 8. The structure in the design region is optimized to achieve the desired transmission properties where function expansion method can easily express the arbitrary optimal structural topology with a relatively small number of design variables. Here, the relative permittivity distribution in the design region can be represented as follows [35]:

$$\varepsilon(x, y) = \varepsilon_a + (\varepsilon_b - \varepsilon_a) H(w(x, y)) \tag{1}$$

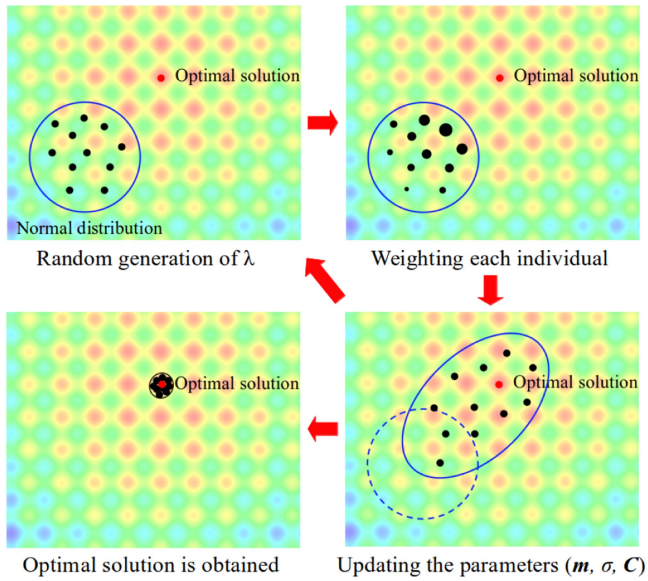

Fig. 9. Image of optimization process in CMA-ES.

where ε_a and ε_b are the relative permittivities of air and dielectric, respectively, and $H(\zeta)$ is the Heaviside function used to binarize the permittivity distribution. $w(x, y)$ is the structure determination function and can be represented using a Fourier series as follows [35]:

$$\begin{aligned} w(x, y) &= \sum_{i=1}^{N_d} c_i f_i(x, y) \\ &= \sum_{i=0}^{N_x - 1} \sum_{j=-N_y}^{N_y - 1} (a_{ij} \cos\theta_{ij} + b_{ij} \sin\theta_{ij}) \\ \theta_{ij} &= \frac{2\pi i}{L_x} x + \frac{2\pi j}{L_y} y \end{aligned} \tag{2}$$

where $f_i(x, y)$ are the basis functions used for structural representation, c_i are the design variables in this problem setting, N_d is the number of design variables, and L_x, L_y are the fundamental periods of Fourier series.

B. Optimization With CMA-ES

In this study, CMA-ES is employed for an efficient optimization of the design variables due to its best convergence behavior in the topology optimal design of NRD guide devices compared to the other existed optimization methods [40]. CMA-ES is a direct search method, where a population of new search points is generated by sampling according to a multivariate normal distribution $\sigma\mathcal{N}(\mathrm{m}, \mathrm{C})$, and then the objective function is evaluated accordingly. The optimization process of CMA-ES is depicted in Fig. 9. Initially the paprameters such as, distribution mean **m**, step size σ and covariance matrix **C** are to be set, and random N individuals are generated according to $\sigma\mathcal{N}(\mathrm{m}, \mathrm{C})$ as follows [41]:

$$N = 4 + 3 \ln N_d. \tag{3}$$

Next, each individual is weighted according to the evaluation value of the objective function as follows [41]:

$$w_i' = \frac{\log(N/2) - \log i}{\sum_{i=0}^{\mu} w_i}$$
$$w_i = \log(N/2) - \log i \tag{4}$$

where $i = 1, 2, \ldots, \mu$ and $\mu = N/2$, utilizing the higher half of individuals to update the parameters. Then, the normal distribution parameters $(\mathbf{m}, \sigma, \mathbf{C})$ are updated using the following equations [41] based on the information of past search points.

$$\mathbf{m} = \mathbf{m} + c_{\mathrm{m}}\sigma\langle\mathbf{y}\rangle_{\mathrm{w}} \tag{5}$$

$$\sigma = \sigma \times \exp\left(\frac{c_\sigma}{d_\sigma}\left(\frac{||\mathbf{p}_\sigma||}{\mathrm{E}||\mathcal{N}(\mathbf{0},\mathbf{I})||} - 1\right)\right) \tag{6}$$

$$\mathbf{C} = \left(1 + c_1\delta(h_\sigma) - c_1 - c_\mu\sum_{j=1}^{\mu} w_j\right)\mathbf{C} + c_1\mathbf{p}_c\mathbf{p}_c^{\mathrm{T}} + c_\mu\sum_{i=1}^{\lambda} w_i\mathbf{y}_{i:N}\mathbf{y}_{i:N}^{\mathrm{T}} \tag{7}$$

where $\langle\mathbf{y}\rangle_{\mathrm{w}} = \sum_{i=1}^{\mu} w_i\mathbf{y}_{i:N}$, and $\mathbf{y}_{i:N}$ is the i-th individual among the N individuals. The values of c_{m}, h_σ, $\mathrm{E}||\mathcal{N}(\mathbf{0},\mathbf{I})||$, step size updating parameters, $\mathbf{p}_\sigma, c_\sigma, d_\sigma$, and covariance matrix updating parameters, $\mathbf{p}_c, c_1, c_\mu$ are considered those given in the literature [41]. Here, the step sizes in the search process are correlated with a mean distribution of the objective function around the search center, where the step sizes are contracted in the directions of convexity while expanding in the other directions. The process is repeated until the global optimal solution is obtained. In this paper, the initial step size and learning rate are set to 0.5 and 1.0, respectively.

C. Propagation Analysis by 2D-FVFEM

The propagation in the given NRD devices during the optimization process is efficiently analyzed by using 2D-FVFEM. We consider a three-dimensional structure of the NRD guide device as shown in Fig. 1(a), where the structure is uniform along the z-direction and the light is propagated along the xy-plane. Then, the functional of propagating behavior for the waveguide analysis can be expressed as follows [38]:

$$F = \iiint\left[(\nabla\times\boldsymbol{H}^*)\cdot\left(\frac{1}{\varepsilon_r}\nabla\times\boldsymbol{H}\right) - k_0^2\boldsymbol{H}^*\cdot\boldsymbol{H}\right]dV - \iint\left\{\boldsymbol{H}^*\cdot\left(\boldsymbol{i}_n\times\frac{1}{\varepsilon_r}\nabla\times\boldsymbol{H}\right)\right\}dS \tag{8}$$

where $\boldsymbol{H}$ is a magnetic field vector, k_0 is a free-space wavenumber and ε_r is a relative permittivity distribution. Here, each component of $\boldsymbol{H}$ can be expressed as follows [38]:

$$H_x = \psi_x(x,y)\cos\left(\frac{\pi}{a}z\right) \tag{9}$$

$$H_y = \psi_y(x,y)\cos\left(\frac{\pi}{a}z\right) \tag{10}$$

$$H_z = \psi_z(x,y)\sin\left(\frac{\pi}{a}z\right) \tag{11}$$

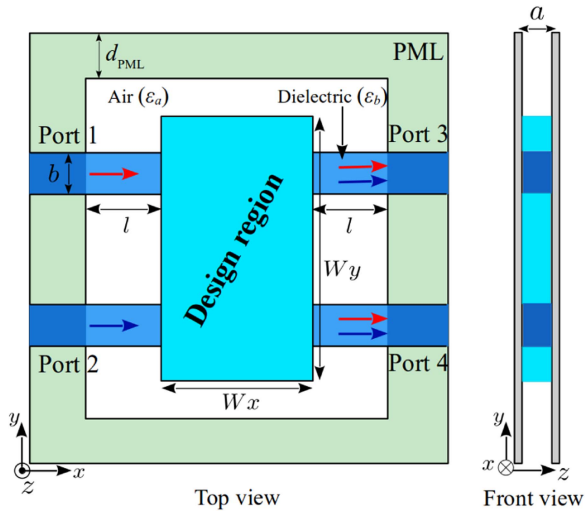

Fig. 10. Design setup of proposed THz NRD rat-race circuit.

Now, discretizing the computational region into edge/nodal hybrid triangular elements [42], [43], and substituting equations (9), (10) and (11) into the functional (8), the final linear equation of FEM can be derived as follows [38]:

$$\left([K] - k_0^2[M]\right)\{\psi\} = [P]\{\psi\} = \{u\} \tag{12}$$

where $[P]$ is a FEM matrix, $\{\psi\}$ is a discretized field and $\{u\}$ is an incidence condition. Finally, both the LSM mode in the input port and LSE mode can be obtained by solving the final FEM equation (12) derived from the full-vectorial expression (8).

IV. Design Examples of NRD Hybrid Devices

We design several THz NRD hybrid devices, including the rat-race circuit and the 90° hybrid device to show the usefulness of our design approach and confirm the significance of the proposed NRD devices over the conventional ones. In the design of these devices, the number of design variables is, $N_d = N_x \times N_y \times 2$, and 400 iterations are considered during the optimization process. THz NRD guide with polyethylene ($\varepsilon_b = 2.3$) as the dielectric material is previously studied in [16] and shows extremely low dielectric and conductor losses in the frequency range around 1 THz. Therefore, polyethylene is used in the design of these compact NRD hybrid devices where the transmission loss is not significant.

A. NRD Rat-Race Circuit

First, we consider the design problem of NRD rat-race circuit as shown in Fig. 10. Table I shows the output description and the design parameters in this design setup. Here, $l = d_{\mathrm{PML}} = 250\,\mu$m and the other structural parameters of the device are same as the parameters considered for conventional NRD rat-race circuit in Section II. The design region size is set to be $W_x \times W_y = 300\,\mu\mathrm{m} \times 840\,\mu\mathrm{m}$ with a 300 μm port separation in the input and output sides to realize a compact optimized device. L_x and L_y should be greater than W_x and W_y, respectively, and are adjusted to $L_x = 1.2W_x$ and $L_y = 1.2W_y$ to prevent the unwanted periodicities in Fourier series. In order to prevent

TABLE I
OUTPUT DESCRIPTION AND THE DESIGN PARAMETERS OF THE PROPOSED NRD RAT-RACE CIRCUIT

Output description	Input port	Output port		Isolated port	
Equal magnitude equal phase	1	3, 4		2	
Equal magnitude opposite phase	2	3, 4		1	
Design parameters					
$a = b$	$l = d_{\mathrm{PML}}$	ε_a	ε_b	W_x	W_y
135 μm	250 μm	1	2.3	300 μm	840 μm

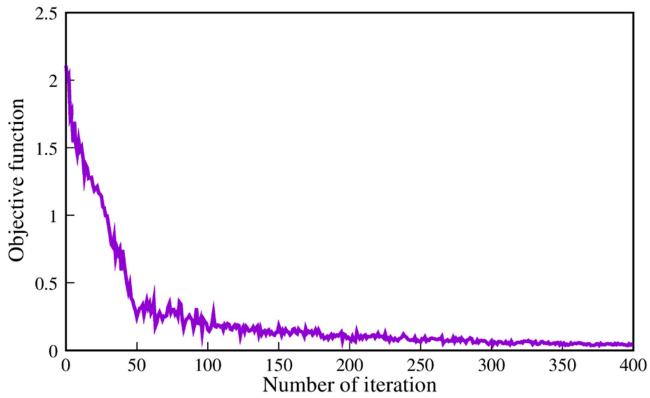

Fig. 11. Convergence behavior in the optimal design of NRD rat-race circuit for single frequency operation at 1 THz.

complex fine structures in optimal devices, it is preferable for N_x and N_y to be smaller, and are set to $N_x = 8$ and $N_y = 12$ in this design problem. The objective function is adjusted to propagate in-phase and 180° out-of-phase power into the output ports 3 and 4 while considering port 1 and port 2 as the incident ports, respectively, for a single frequency operation at 1 THz as follows:

$$\begin{aligned} &\text{Minimize}\, C = C_1 + C_2 \\ C_1 &= \left|2 - |S_{31}|^2 - |S_{41}|^2 - |S_{32}|^2 - |S_{42}|^2\right| \\ &\quad + \left|\mathrm{Max}_{kl}\left(|S_{kl}|^2\right) - \mathrm{Min}_{kl}\left(|S_{kl}|^2\right)\right| \\ C_2 &= \frac{\left|\mathrm{Max}_{kl}\left(\theta_{kl}\right) - \mathrm{Min}_{kl}\left(\theta_{kl}\right)\right|}{180^\circ} \\ \theta_{31/41/32} &= \arg[S_{31/41/32}], \theta_{42} = \arg[S_{42}] + 180^\circ \end{aligned} \tag{13}$$

where $k = 3, 4$ and $l = 1, 2$. The convergence behavior of the objective function in this optimal design is shown in Fig. 11. As we can see in the figure, 400 iterations of device optimization are sufficient to reach the optimal solution. Fig. 12 shows the propagation fields in the optimized structure where the optimal device accomplishes the rat-race circuit function with almost ideal transmission properties for both the incident ports 1 and 2. At output ports 3 and 4, the achieved in-phase transmission power is 50.6% and 49.4% with phase angles of 146.8 and 147.2 degrees, respectively, whereas the 180° out-of-phase power is 49.4% and 48.9% with phase angles of 146.9 and −32.7 degrees, respectively. The frequency characteristics of the optimized

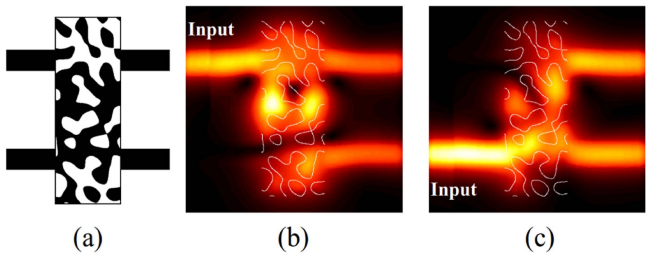

Fig. 12. Optimized results of NRD rat-race at single frequency operation, (a) optimized structure, (b) and (c) propagation fields when port 1 and port 2 are the incident ports, respectively.

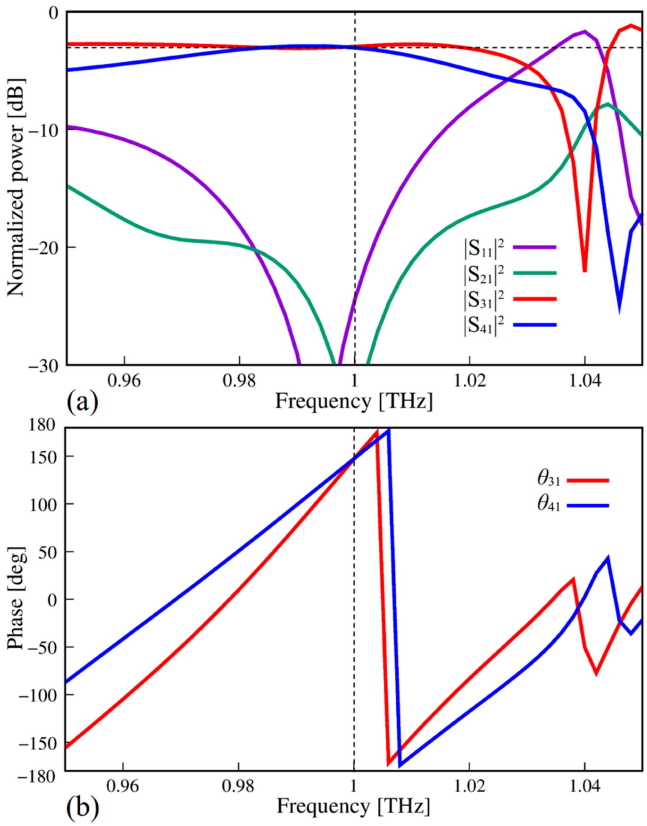

Fig. 13. Frequency characteristics of the designed NRD rat-race at single frequency operation when port 1 is input, (a) normalized power, and (b) phase angle.

device for incident ports 1 and 2, respectively, are shown in Figs. 13 and 14. The figures demonstrate that the desired output results at 1 THz are obtained with in-phase and 179.6° out-of-phase characteristics. The obtained reflections for both the incident ports 1 and 2 are lower than −20 dB. Furthermore, the appearance of LSE_{01} mode at the output ports is greatly reduced to far lower than −20 dB.

In order to realize the broad bandwidth characteristics of NRD rat-race, we increase the design region size to be $W_x \times W_y = 400\ \mu\mathrm{m} \times 1040\ \mu\mathrm{m}$ with a 500 μm port separation in the input and output sides. The values for N_x and N_y are respectively adjusted to 8 and 8, while the remaining structural parameters are left unchanged from the single frequency operation. The

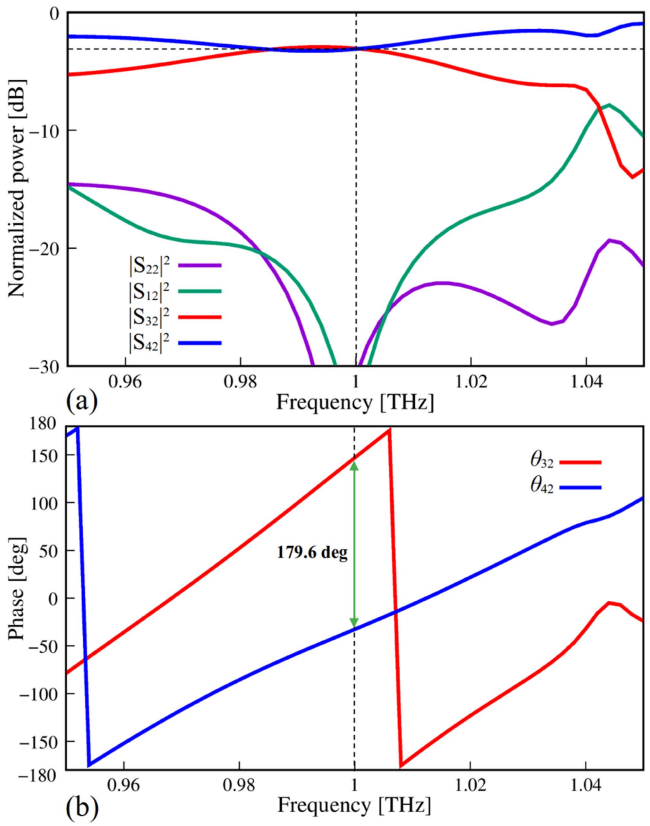

Fig. 14. Frequency characteristics of the designed NRD rat-race at single frequency operation when port 2 is input, (a) normalized power, and (b) phase angle.

objective function is modified to evaluate the device structure at five distinct frequencies, 0.95, 0.975, 1.0, 1.025 and 1.05 THz, and is given by

$$\text{Minimize}\, C = \sum_{i=1}^{5} \left(C_1\left(f_i\right) + C_2\left(f_i\right)\right)$$

$$C_1\left(f_i\right) = \sum_{l=1}^{2}\sum_{k=3}^{4}\left|\frac{1}{2} - \left|S_{kl}\left(f_i\right)\right|^2\right| \tag{14}$$

$$C_2\left(f_i\right) = \frac{\left|\text{Max}_{kl}\left(\theta_{kl}\left(f_i\right)\right) - \text{Min}_{kl}\left(\theta_{kl}\left(f_i\right)\right)\right|}{180^\circ}$$

$$\theta_{31/41/32} = \arg[S_{31/41/32}], \theta_{42} = \arg[S_{42}] + 180^\circ$$

$$\left(f_{1,2,3,4,5} = 0.95, 0.975, 1.0, 1.025, 1.05\,\text{THz}\right).$$

Fig. 15 shows the optimized structure and propagation fields in the optimized NRD rat-race at broadband operation. In the figure it is shown that the power at the output ports, 3 and 4 is almost equally splitted for both the incident ports, 1 and 2. Furthermore, the optimized device achieved a broad bandwidth of almost 100 GHz at the aimed frequency range with almost constant in-phase and 180° out-of-phase characteristics as depicted in Figs. 16 and 17. Although the reflections at the incident ports 1 and 2 are slightly increased from the single frequency operation, yet they are considerably lower than −15 dB. Here, the LSE_{01} mode at the output ports is around −20 dB.

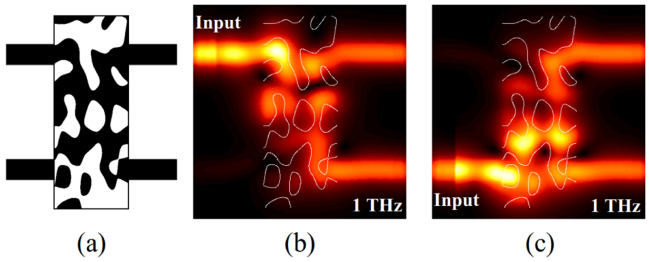

Fig. 15. Optimized results of NRD rat-race at broadband operation, (a) optimized structure, (b) and (c) propagation fields when port 1 and port 2 are the incident ports, respectively.

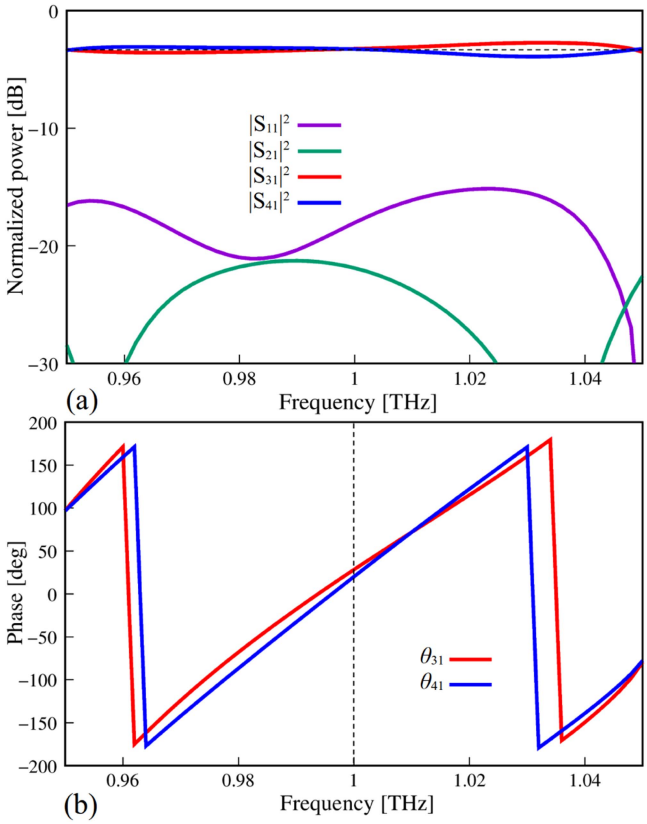

Fig. 16. Frequency characteristics of the designed NRD rat-race at broadband operation when port 1 is input, (a) normalized power, and (b) phase angle.

These results demonstrate that the proposed method solves the difficulty of an undesired LSE_{01} mode arising in the output ports while realizing conventional NRD rat-race device in Section II with a 108 μm reduction in device size, whereas the outer circle ring diameter of the conventional device was 1148 μm. Therefore, it is seen that realizing the proposed THz NRD rat-race circuit significantly improves the device performance in comparison with the conventional NRD rat-race devices.

B. NRD 90° Hybrid Device

In addition to the NRD rat-race, NRD 90° hybrid device also has the practical applications in the design of THz-wave integrated circuits and is usually used in signal splitting conditions

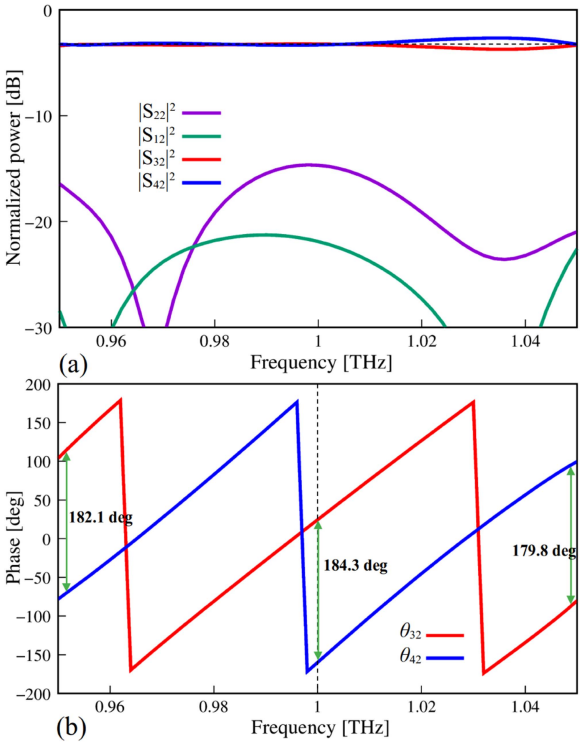

Fig. 17. Frequency characteristics of the designed NRD rat-race at broadband operation when port 2 is input, (a) normalized power, and (b) phase angle.

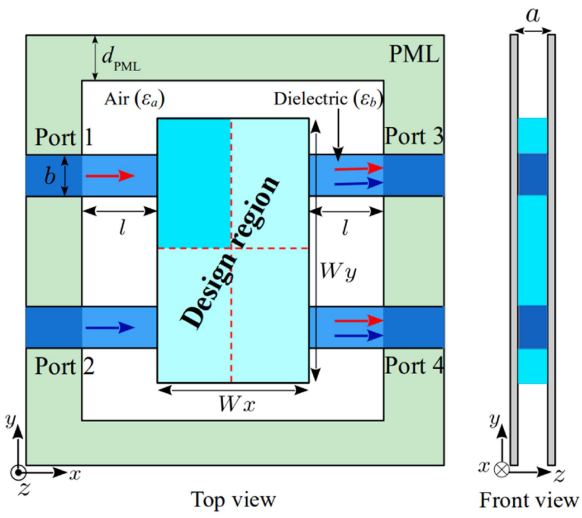

Fig. 18. Design setup of proposed THz NRD 90° hybrid device.

when undesired reflections might potentially cause circuit damage [44], [45], [46]. Therefore, we consider a design problem of the THz NRD 90° hybrid device as shown in Fig. 18. The output description of the design problem is shown in Table II. With this design setup, equal magnitude power with 90° phase difference can be obtained at the output ports, 3 and 4 for both the incident ports, 1 and 2 with a strong non-operating input port isolation. Here, the design region size is again set to $W_x \times W_y = 300\ \mu$m $\times 840\ \mu$m with a 300 μm port separation in the input and output sides. One-four symmetric condition is applied in the design

TABLE II
OUTPUT DESCRIPTION OF THE PROPOSED NRD 90° HYBRID DEVICE

Output description	Input port	Output port	Isolated port
Equal magnitude	1	3, 4	2
90° phase difference	2	3, 4	1

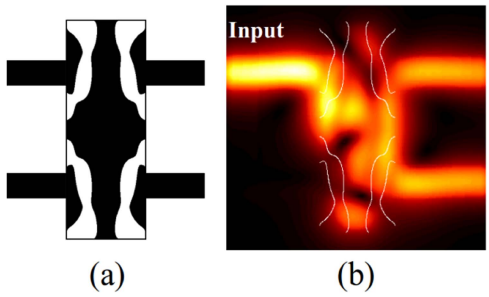

Fig. 19. Optimized results of NRD 90° hybrid device at single frequency operation, (a) optimized structure, and (b) propagation field.

region along x and y-axis indicated by red line in the figure. Since only one-fourth of the design region is optimized, N_x and N_y are adjusted to 6 and 6, respectively. In this case, the S-parameter of the 90° hybrid device is represented as follows:

$$\begin{bmatrix} b_1 \\ b_2 \\ b_3 \\ b_4 \end{bmatrix} = \begin{bmatrix} 0 & 0 & \frac{1}{\sqrt{2}} & \frac{e^{j\theta}}{\sqrt{2}} \\ 0 & 0 & \frac{e^{j\theta}}{\sqrt{2}} & \frac{1}{\sqrt{2}} \\ \frac{1}{\sqrt{2}} & \frac{e^{j\theta}}{\sqrt{2}} & 0 & 0 \\ \frac{e^{j\theta}}{\sqrt{2}} & \frac{1}{\sqrt{2}} & 0 & 0 \end{bmatrix} \begin{bmatrix} a_1 \\ a_2 \\ a_3 \\ a_4 \end{bmatrix} \tag{15}$$

with

$$\theta = \pm\frac{\pi}{2}$$

where $S_{31} = S_{42}$ and $S_{41} = S_{32}$. Then, in order to obtain equal magnitude with 90° phase difference in the output ports, the objective function is simply modified as follows:

$$\text{Minimize}\, C = \sum_{j=1}^{2}\sum_{i=3}^{4}\left|\frac{1}{2} - |S_{ij}|^2\right| \tag{16}$$

The other design parameters are set to be same as the previous design examples. The output results of 90° hybrid device presented in this paper are for incident port 1, and because of the applied symmetric condition, the results are identical for incident port 2 as well. Fig. 19 shows the optimized structure and the propagation field of the designed NRD 90° hybrid device at single frequency operation. The optimal structure achieved an almost ideal transmission property propagated equally into the output ports, 3 and 4 with 49.8% of power transmission, where the phase angles are 7.2 and 96.3 degrees, respectively. As shown in Fig. 20, the frequency characteristics of the optimized device demonstrate the intended output characteristics at 1 THz with 89.1° of phase difference and a far lower reflection than −20 dB. The obtained LSE_{01} mode at the output ports is far lower than −20 dB.

For broadband operation of the device, we increase the design region size to be $W_x \times W_y = 400\ \mu$m $\times 1040\ \mu$m with a

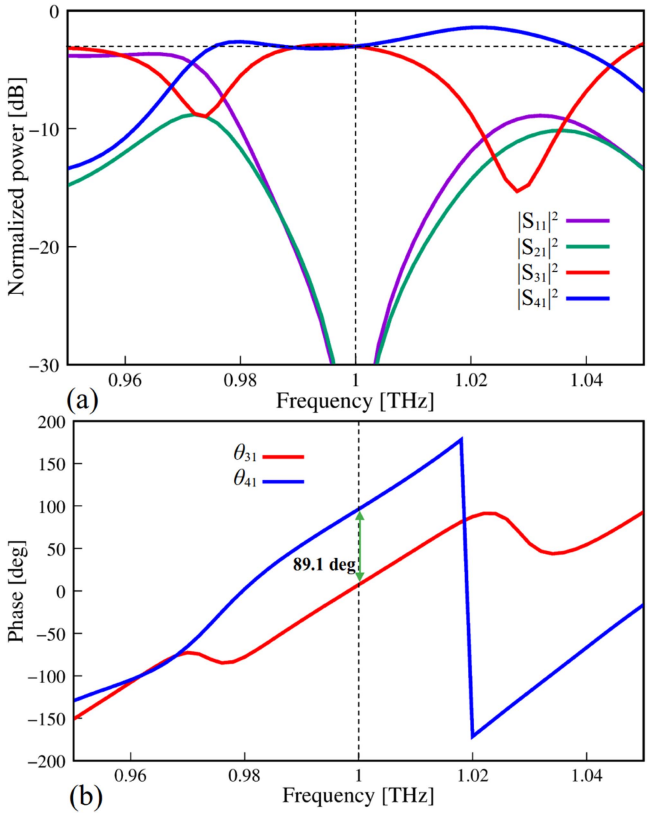

Fig. 20. Frequency characteristics of the designed NRD 90° hybrid device at single frequency operation, (a) normalized power, and (b) phase angle.

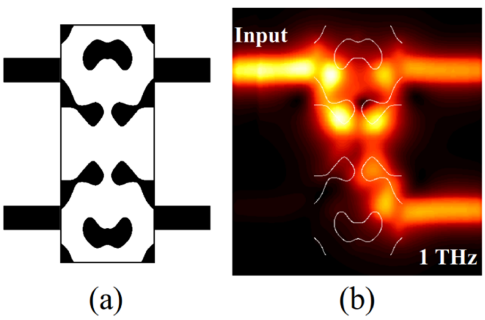

Fig. 21. Optimized results of NRD 90° hybrid device at broadband operation, (a) optimized structure, and (b) propagation field.

500 μm port separation, as of the NRD rat-race circuit. All the other design parameters are considered to be the same as those of single frequency operation. The objective function is modified to evaluate the device structure at three distinct frequencies, 0.975, 1.0 and 1.025 THz, as follows:

$$\text{Minimize}\, C = \sum_{i=1}^{3}\sum_{k=1}^{2}\sum_{j=3}^{4}\left|\frac{1}{2} - |S_{jk}(f_i)|^2\right| \qquad (17)$$

$$(f_{1,2,3} = 0.975, 1.0, 1.025\,\text{THz}).$$

The optimal structure and propagation field of the NRD 90° hybrid device at broadband operation are depicted in Fig. 21. The optimized structure obtained a broad bandwidth of about 90 GHz around the targeted frequency range with almost constant 90°

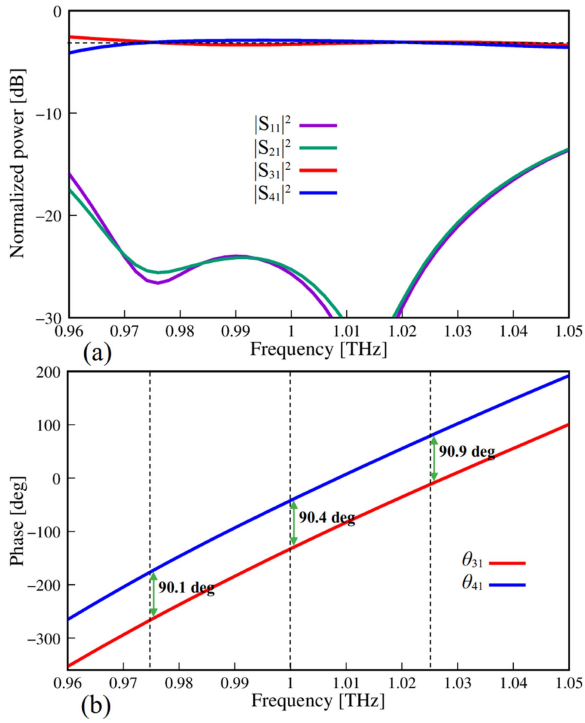

Fig. 22. Frequency characteristics of the designed NRD 90° hybrid device at broadband operation, (a) normalized power, and (b) phase angle.

phase difference, as shown from the frequency characteristics of the device in Fig. 22. The obtained reflection at the targeted frequency range is lower than −20 dB, though the reflection at the lower and higher frequency sides is considerably around −15 dB. Here, lower than −20 dB of LSE_{01} mode appears at the output ports of the device.

V. Fabrication Tolerance

So far, we have designed THz NRD hybrid devices, rat-race circuit and 90° hybrid device at single frequency and broadband operations. In this section, the fabrication tolerance of these proposed devices is discussed in terms of structural deviation effect on the output power and phase angles. Here, the topological structure of the devices is considered to be expanded or shrunk, and the image of the expansion and contraction of the structure is shown in Fig. 23. Considering structure determination function (2) discussed in Section III, the structure after the change can be represented as follows:

$$w'(x,y) = w(x,y) + \delta\,|\nabla w(x,y)| \qquad (18)$$

where $\nabla w(x,y)$ is the gradient vector of $w(x,y)$, and the core region shrinks when $\delta < 0$ and expands when $\delta > 0$. In this case, we optimize the first design example of proposed NRD rat-race again considering the fabrication tolerance in the objective function. This device has a comparatively fine structure than the other designed NRD hybrid devices. Here, N_x and N_y are set to 8 and 8, respectively, while all the other design parameters remain unchanged. The objective function is modified to take into consider three different structures with structural deviations

Fig. 23. Image of structural tolerance consideration of the optimized devices (red indicates expansion, green indicates contraction and blue is the original structure).

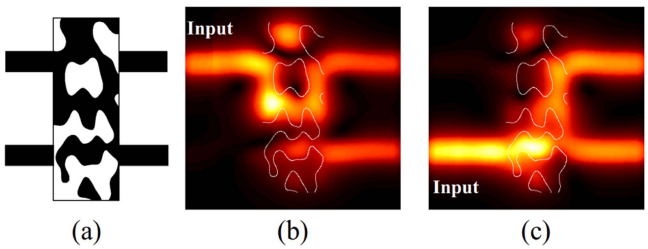

Fig. 24. Optimized results of NRD rat-race with fabrication tolerance consideration, (a) optimized structure, (b) and (c) propagation fields when port 1 and port 2 are the incident ports, respectively.

TABLE III
COMPARISON OF THE PROPOSED NRD RAT-RACE CIRCUIT WITH EXISTED LITERATURE IN THE SIMILAR KIND OF WAVEGUIDE PLATFORMS

Ref.	Dev. size (μm)	Operating freq. (THz)	Trans. loss (dB)	Bandwidth (GHz)
[18]	540	0.34	-3.2	10
This work (Conventional)	1148	1	-6.1	—
This work (Proposed)	1040	1	-3.06	50

of $+3$, 0 and -3 μm, as follows:

$$\text{Minimize}\, C = \sum_{i=1}^{3} \left(C_1\left(\delta_i\right) + C_2\left(\delta_i\right)\right)$$

$$C_1\left(\delta_i\right) = \sum_{l=1}^{2}\sum_{k=3}^{4}\left|\frac{1}{2} - \left|S_{kl}\left(\delta_i\right)\right|^2\right| \tag{19}$$

$$C_2\left(\delta_i\right) = \frac{\left|\text{Max}_{kl}\left(\theta_{kl}\left(\delta_i\right)\right) - \text{Min}_{kl}\left(\theta_{kl}\left(\delta_i\right)\right)\right|}{180^\circ}$$

$$\theta_{31/41/32} = \arg[S_{31/41/32}], \theta_{42} = \arg[S_{42}] + 180^\circ$$

$$(\delta_{1,2,3} = +3, 0, -3\,\mu\text{m}).$$

After optimization, a simplified structure with almost ideal transmission properties is obtained compared to the device designed without fabrication tolerance, as shown in Fig. 24. The obtained transmission power for incident port 1 at the output ports 3 and 4, is 49.7% and 49.2% with phase angles of 108.1 and 107.8 degrees, respectively. For incident port 2,

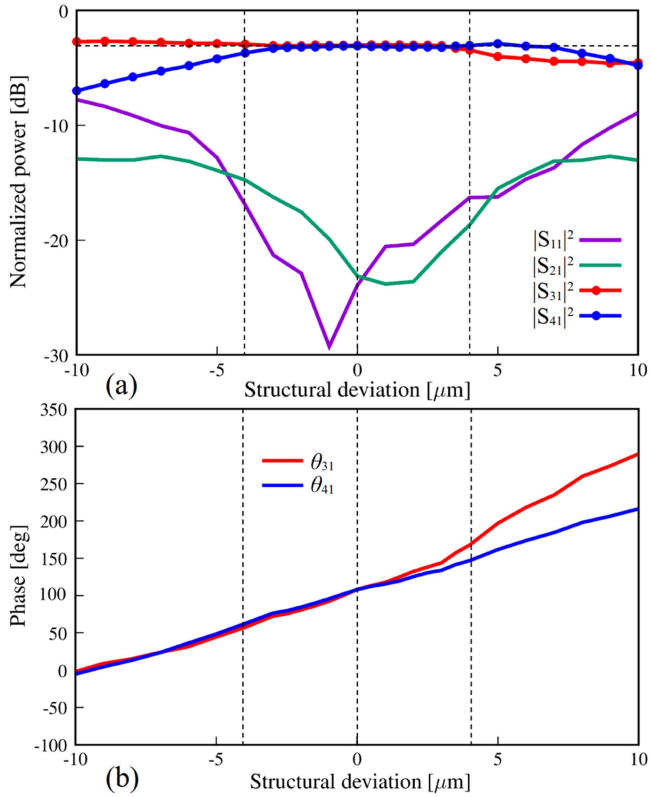

Fig. 25. Effect of structural deviation (port 1 is input) on (a) transmitted power into the output ports and (b) phase angle.

49.3% and 47.7% it is with phase angles of 109.7 and -70.4 degrees, respectively. The reflections for both the incident ports 1 and 2 are obtained lower than -20 dB. Figs. 25 and 26 show the structural deviation effect on the transmitted output power and phase angles within the deviation range of ± 10 μm. In the figures, it is shown that the output power at ports 3 and 4 is nearly constant up to the ± 4 μm of structural deviation and it deviates if the structure is even more deviated for both the incident ports, 1 and 2. Here, the structural shrink has a higher output power deviation compared to the structural expansion. The phase angles of output power for the incident port 1 almost remain in-phase with the shrink in structure and considerably deviated after 4 μm of structural expansion. For incident port 2, the phase difference decreases with the structural shrink and it increases with the expansion of the structure. The phase difference decreases to 167.8° from the obtained 180.1° for -4 μm of structural deviation, whereas it increases to 197.6° for the structural expansion of 4 μm. The reflections for both the incident ports 1 and 2 increase with the structural deviation and for ± 4 μm of deviation reflections are around or lower than -15 dB. From the analysis, we can see that the targeted structural tolerance with the desired output results is obtained and ± 4 μm structural deviation may be tolerable during the fabrication of the devices considering the required phase angle, reflection and output power. Figs. 27 and 28 show the I/O port width deviation effect on the transmitted output power and phase angles within the deviation range of ± 10 μm. As we can see, the output results for both the incident ports 1 and 2 are almost consistent regardless of the port width deviation. Therefore, deviation in port

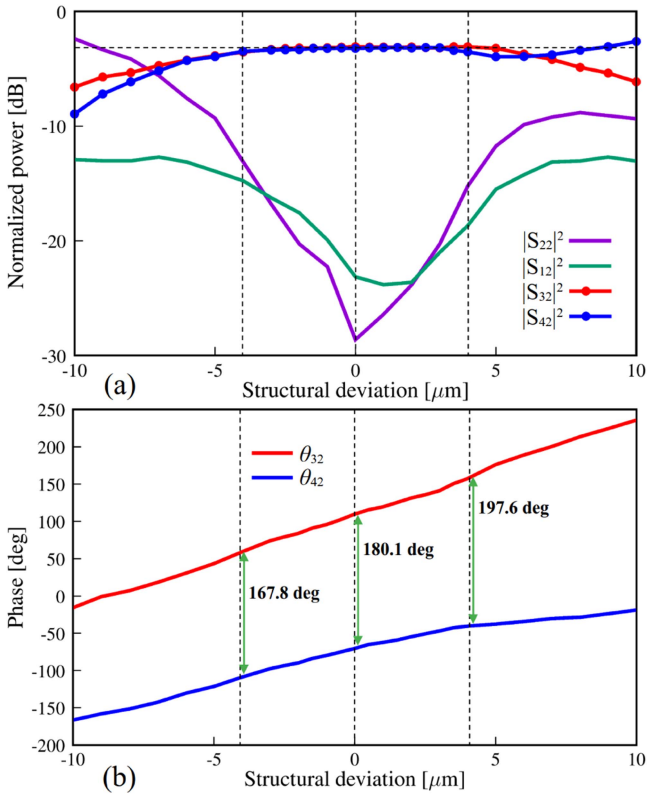

Fig. 26. Effect of structural deviation (port 2 is input) on (a) transmitted power into the output ports and (b) phase angle.

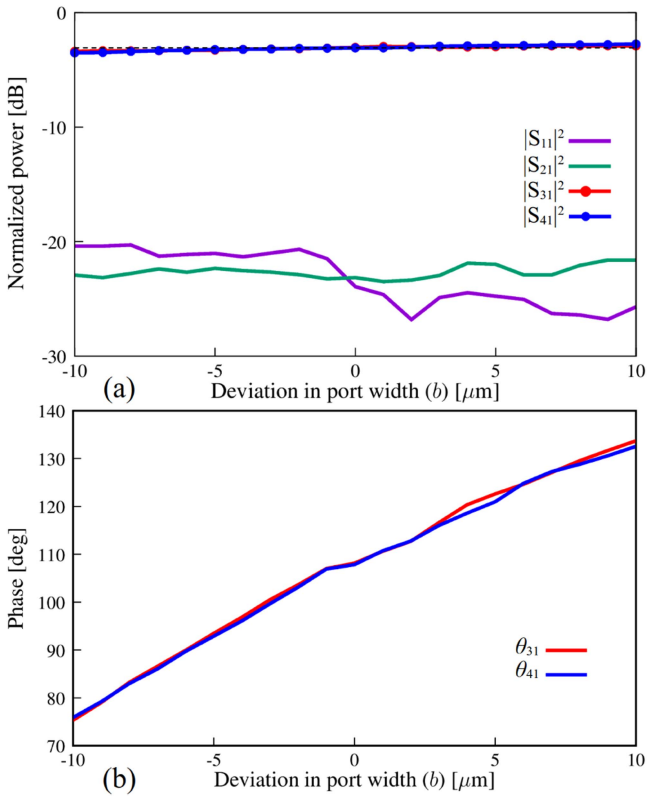

Fig. 27. Effect of port width (b) deviation (port 1 is input) on (a) transmitted power into the output ports and (b) phase angle.

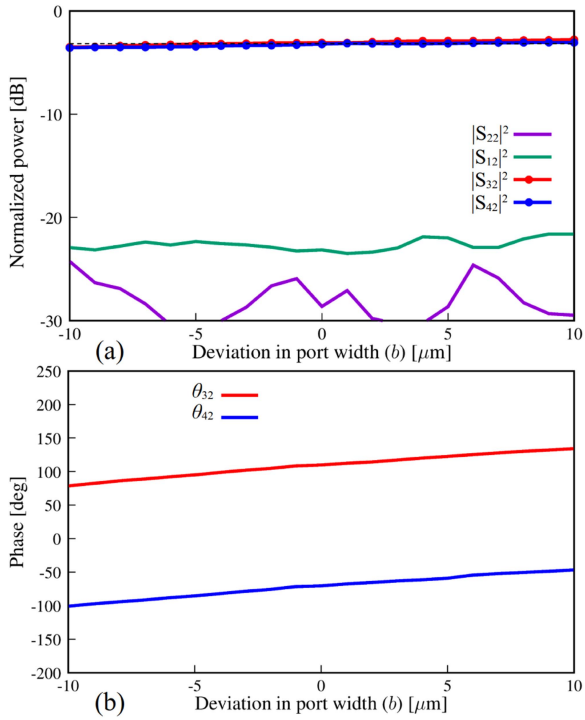

Fig. 28. Effect of port width (b) deviation (port 1 is input) on (a) transmitted power into the output ports and (b) phase angle.

width within the considerable range may not have a significant effect on the performance of the proposed devices. Table III demonstrates a comparison of the proposed NRD rat-race circuit with the existed literature in different similar kind of waveguide platforms.

VI. Conclusion

In this paper, we proposed topology optimal design of THz NRD rat-race circuit based on function expansion method and CMA-ES. The difficulty in realizing conventional NRD rat-race circuits because of appearing unwanted LSE_{01} mode in the output ports has been studied at the beginning of the paper. Then, the usefulness of our optimal design approach and the significance of the proposed THz NRD devices over the conventional ones are confirmed by designing several NRD hybrid devices, rat-race circuit and 90° hybrid device. The proposed method overcomes the difficulty of appearing unwanted LSE_{01} mode in realizing conventional NRD rat-race devices with a reduced device size by 108 μm. The proposed NRD devices achieved the desired transmission properties at the both single frequency and broadband operations, and a significant improvement in the device performance of THz NRD rat-race circuit is confirmed in comparison with the conventional NRD rat-race devices. Finally, the fabrication tolerance of the proposed devices in terms of structural deviation effect on the output power and phase angles has been discussed in detail. In our future work, we will further discuss the design of THz NRD rat-race circuit considering the conductor loss and practical fabrication. Moreover, we would like to investigate more different types of NRD devices for THz applications and improve our design strategy.

REFERENCES

[1] P. H. Siegel, "Terahertz technology," *IEEE Trans. Microw. Theory Tech.*, vol. 50, no. 3, pp. 910–928, Mar. 2002.

[2] I. F. Akyildiz, J. M. Jornet, and C. Han, "Terahertz band: Next frontier for wireless commnuications," *Phys. Commun.*, vol. 12, pp. 16–32, 2014.

[3] Z. Chen et al., "Terahertz wireless communications for 2030 and beyond: A cutting-edge frontier," *IEEE Commun. Mag.*, vol. 59, no. 11, pp. 66–72, Nov. 2021.

[4] H. Xiong, Q. Ji, T. Bashir, and F. Yang, "Dual-controlled broadband terahertz absorber based on graphene and Dirac semimetal," *Opt. Exp.*, vol. 28, no. 9, pp. 13884–94, Apr. 2020.

[5] P. H. Siegel, "Terahertz technology in biology and medicine," *IEEE Trans. Microw. Theory Tech.*, vol. 52, no. 10, pp. 2438–2447, Oct. 2004.

[6] R. Zhou, C. Wang, W. Xu, and L. Xie, "Biological applications of terahertz technology based on nanomaterials and nanostructures," *Nanoscale*, vol. 11, no. 8, pp. 3445–3457, 2019.

[7] B. Clough, J. Liu, and X. C. Zhang, "'All air-plasma' terahertz spectroscopy," *Opt. Lett.*, vol. 36, no. 13, pp. 2399–2401, 2011.

[8] J. F. Federici et al., "THz imaging and sensing for security applications–explosives, weapons and drugs," *Semicond. Sci. Technol.*, vol. 20, no. 7, pp. S266–S280, 2005.

[9] Y. A. García-Jomaso, D. L. Hernández-Roa, J. Garduño-Mejía, C. G. Treviño-Palacios, O. V. Kolokoltsev, and N. Qureshi, "Sub-wavelength continuous THz imaging system based on interferometric detection," *Opt. Exp.*, vol. 29, no. 12, pp. 19120–19125, 2021.

[10] C. D. Nordquist, M. C. Wanke, A. M. Rowen, C. L. Arrington, M. Lee, and A. D. Grine, "Design, fabrication, and characterization of metal micromachined rectangular waveguides at 3 THz," in *Proc. IEEE Antennas Propag. Soc. Int. Symp*., 2008, pp. 1–4.

[11] K. Jia, L. Fan, and Z. Cao, "THz narrow band-pass filter based on stop-band modulation in corrugated parallel plate waveguides," *Opt. Commun.*, vol. 465, 2020, Art. no. 125604.

[12] G. K. C. Kwan and N. K. Das, "Excitation of a parallel-plate dielectric waveguide using a coaxial probe-basic characteristics and experiments," *IEEE Trans. Microw. Theory Techn.*, vol. 50, no. 6, pp. 1609–1620, Jun. 2002.

[13] M. I. H. Patwary, A. Iguchi, and Y. Tsuji, "Efficient optimal design of mosaic-like PPDW devices for THz application using the adjoint variable method," *Opt. Exp.*, vol. 31, no. 10, pp. 16593–16606, 2023.

[14] T. Yoneyama and S. Nishida, "Nonradiative dielectric waveguide for millimeter-wave integrated circuits," *IEEE Trans. Microw. Theory Techn.*, vol. 29, no. 11, pp. 1188–1192, Nov. 1981.

[15] T. Yoneyama and S. Nishida, "Nonradiative Dielectric Waveguide," in *Infrared and Millimeter Waves*, K. J. Button, Ed. Cambridge, MA, USA: Academic Press, 1984, pp. 61–98.

[16] M. I. H. Patwary, A. Iguchi, and Y. Tsuji, "Optimal design of NRD grating bandpass filters for THz application using GA and EIM," *IEEE Photon. J.*, vol. 16, no. 1, Feb. 2024, Art no. 7700109.

[17] T. Bashir, M. I. H. Patwary, K. Morimoto, A. Iguchi, Y. Tsuji, and T. Kashiwa, "Guided mode analysis of NRD guide using efficient FEM with impedance boundary conditions for THz applications," *J. Lightw. Technol.*, vol. 42, no. 9, pp. 3320–3329, May 2024.

[18] X. Yang, Y. Fan, B. Zhang, L. Ye, and X. Xu, "A novel terahertz rat-race hybrid coupler based on PPDW," *J. Infrared, Millimeter, Terahertz Waves*, vol. 32, pp. 1291–1298, 2011.

[19] M. El Khaldi, F. Podevin, O. Exshaw, A. Vilcot, and A. M. E. Safwat, "Improvement of performance of optically controlled microstrip phase shifters," *IET Microw., Antennas Propag.*, vol. 1, no. 2, pp. 427–432, 2007.

[20] Y. J. Yang, J. X. Chen, and Z. H. Bao, "Broadband compact rat-race hybrid and its application to mixers," *IET Microw., Antennas Propag.*, vol. 4, no. 12, pp. 2001–2007, 2010.

[21] M. A. Gozel, M. Kahriman, and O. Kasar, "Design of an efficiency-enhanced greinacher rectifier operating in the GSM 1800 band by using rat-race coupler for RF energy harvesting applications," *Int. J. RF Microw. Comput.-Aided Eng.*, vol. 29, no. 1, 2019, Art. no. e21621.

[22] A. M. Zaidi et al., "A dual-band rat-race coupler for high band ratio wireless applications," *IEEE Trans. Instrum. Meas.*, vol. 70, 2021, Art no. 2006806.

[23] J. Muñoz-Enano, P. Vélez, M. Gil Barba, J. Mata-Contreras, and F. Martín, "Differential-mode to common-mode conversion detector based on rat-race hybrid couplers: Analysis and application to differential sensors and comparators," *IEEE Trans. Microw. Theory Techn.*, vol. 68, no. 4, pp. 1312–1325, Apr. 2020.

[24] D. Marcuse, "Length optimization of an S-shaped transition between offset optical waveguides," *Appl. Opt.*, vol. 17, no. 5, pp. 763–768, 1978.

[25] A. Iguchi, Y. Tsuji, T. Yasui, and K. Hirayama, "Efficient shape and topology optimization based on sensitivity analysis for optical waveguide devices utilizing full-vectorial BPM," *J. Lightw. Technol.*, vol. 38, no. 8, pp. 2328–2335, Apr. 2020.

[26] T. Bashir, K. Morimoto, A. Iguchi, Y. Tsuji, and T. Kashiwa, "Mosaic based optimization of NRD guide devices using binary evolutionary approaches and 2D-FVFEM," *IEEE Access*, vol. 10, pp. 60682–60695, 2022.

[27] T. Fujisawa and K. Saitoh, "Bayesian direct-binary-search algorithm for the efficient design of mosaic-based power splitters," *OSA Continuum*, vol. 4, no. 4, pp. 1258–1270, 2021.

[28] T. Bashir, K. Morimoto, A. Iguchi, Y. Tsuji, T. Kashiwa, and S. Nishiwaki, "Optimal design of broadband non-radiative dielectric guide devices using binary genetic algorithm and 2D-FVFEM," *Int. J. Numer. Modelling*, vol. 35, no. 4, 2022, Art. no. e2984.

[29] S. Molesky, Z. Lin, A. Y. Piggott, W. Jin, J. Vucković, and A. W. Rodriguez, "Inverse design in nanophotonics," *Nature Photon.*, vol. 12, no. 11, pp. 659–670, Nov. 2018.

[30] Y. Tsuji, K. Hirayama, T. Nomura, K. Sato, and S. Nishiwaki, "Design of optical circuit devices based on topology optimization," *IEEE Photon. Technol. Lett.*, vol. 18, no. 7, pp. 850–852, Apr. 2006.

[31] J. S. Jensen and O. Sigmund, "Systematic design of photonic crystal structures using topology optimization: Low-loss waveguide bends," *Appl. Phys. Lett.*, vol. 84, pp. 2022–2024, Mar. 2003.

[32] K. Morimoto, A. Iguchi, and Y. Tsuji, "Efficient topology optimization of optical waveguide using finite element method based on slowly varying envelope approximation," *Optik*, vol. 226, 2021, Art. no. 165951.

[33] N. Hieda, K. Morimoto, A. Iguchi, Y. Tsuji, and T. Kashiwa, "Topology optimal design of NRD guide devices using function expansion method and evolutionary approaches," *IEICE Trans. Electron.*, vol. E105-C, no. 11, pp. 652–659, 2022.

[34] A. Koda, K. Morimoto, and Y. Tsuji, "A study on topology optimization of plasmonic waveguide devices using function expansion method and evolutionary approach," *J. Lightw. Technol.*, vol. 37, no. 3, pp. 981–988, Feb. 2019.

[35] Y. Tsuji and K. Hirayama, "Design of optical circuit devices using topology optimization method with function-expansion-based refractive index distribution," *IEEE Photon. Technol. Lett.*, vol. 20, no. 12, pp. 982–984, Jun. 2008.

[36] T. Yasui, Y. Tsuji, J. Sugisaka, and K. Hirayama, "Design of three-dimensional optical circuit devices by using topology optimization method with function-expansion-based refractive index distribution," *J. Lightw. Techol.*, vol. 31, no. 23, pp. 3765–3770, Dec. 2013.

[37] N. Hansen and A. Ostermeier, "Adapting arbitary normal mutation distributions in evolution strategies: The covariance matrix adaptation," in *Proc. IEEE Int. Conf. Evol. Comput.*, 1996, pp. 312–317.

[38] Y. Tsuji, K. Morimoto, A. Iguchi, T. Kashiwa, and S. Nishiwaki, "Two-dimensional full-vectorial finite element analysis of NRD guide devices," *IEEE Microw. Wireless Compon. Lett.*, vol. 31, no. 4, pp. 345–348, Apr. 2021.

[39] H. -X. Xu, G. -M. Wang, and K. Lu, "Microstrip rat-race couplers," *IEEE Microw. Mag.*, vol. 12, no. 4, pp. 117–129, Jun. 2011.

[40] N. Hieda, A. Iguchi, Y. Tsuji, K. Morimoto, and T. Kashiwa, "Topology optimization of NRD guide devices using covariance matrix adaptation evolution strategy," in *Proc. IEEE Asia-Pacific Microw. Conf.*, 2022, pp. 387-389.

[41] N. Hansen, "The CMA evolution strategy: A tutorial," 2016, *arXiv:1604.00772*.

[42] J.-F. Lee, D.-K. Sun, and Z. J. Cendes, "Full-wave analysis of dielectric waveguides using tangential vector finite elements," *IEEE Trans. Microw. Theory Techn.*, vol. 39, no. 8, pp. 1262–1271, Aug. 1991.

[43] M. Koshiba and Y. Tsuji, "Curvilinear hybrid edge/nodal elements with triangular shape for guided-wave problems," *J. Lightw. Technol.*, vol. 18, no. 5, pp. 737–743, May 2000.

[44] S. Liu et al., "Silicon micromachined waveguide quadrature-hybrid coupler at terahertz frequency band," *J. Infrared, Millimeter, Terahertz Waves*, vol. 36, pp. 709–719, 2015.

[45] B. Zhang et al., "Four-hundred gigahertz broadband multi-branch waveguide coupler," *IET Microw., Antennas Propag.*, vol. 14, no. 11, pp. 1175–1179, Apr. 2020.

[46] C. Li and Y. Cheng, "Terahertz couplers based on branch lines and waveguide resonators," *Microw. Opt. Techn. Lett.*, vol. 66, no. 1, Jan. 2024, Art. no. e34021.